Simulation of the Enzyme Reaction Mechanism of Malate Dehydrogenase[†]

Mark A. Cunningham,[‡,§] L. Lawrence Ho,[‡,||] Dzung T. Nguyen,[⊥] Richard E. Gillilan,[#] and Paul A. Bash*,[‡]

Center for Mechanistic Biology and Biotechnology, Argonne National Laboratory, Argonne, Illinois 60439, M. A. Cunningham Associates, Northbrook, Illinois 60062, J. W. Gibbs Laboratory, Department of Physics, Yale University, New Haven, Connecticut 06511, InPharmatics Corporation, San Diego, California 92126, and Cornell Theory Center, Cornell University, Ithaca, New York 14853

Received November 1, 1996; Revised Manuscript Received January 21, 1997[⊗]

ABSTRACT: A hybrid numerical method, which employs molecular mechanics to describe the bulk of the solvent−protein matrix and a semiempirical quantum-mechanical treatment for atoms near the reactive site, was utilized to simulate the minimum energy surface and reaction pathway for the interconversion of malate and oxaloacetate catalyzed by the enzyme malate dehydrogenase (MDH). A reaction mechanism for proton and hydride transfers associated with MDH and cofactor nicotinamide adenine dinucleotide (NAD) is deduced from the topology of the calculated energy surface. The proposed mechanism consists of (1) a sequential reaction with proton transfer preceding hydride transfer (malate to oxaloacetate direction), (2) the existence of two transition states with energy barriers of approximately 7 and 15 kcal/mol for the proton and hydride transfers, respectively, and (3) reactant (malate) and product (oxaloacetate) states that are nearly isoenergetic. Simulation analysis of the calculated energy profile shows that solvent effects due to the protein matrix dramatically alter the intrinsic reactivity of the functional groups involved in the MDH reaction, resulting in energetics similar to that found in aqueous solution. An energy decomposition analysis indicates that specific MDH residues (Arg-81, Arg-87, Asn-119, Asp-150, and Arg-153) in the vicinity of the substrate make significant energetic contributions to the stabilization of proton transfer and destabilization of hydride transfer. This suggests that these amino acids play an important role in the catalytic properties of MDH.

A fundamental property of biological organisms is their ability to transform simple organic molecules into unique biochemical components with great efficiency and specificity. The catalysts of these transformations, complex biological molecules known as enzymes, have extraordinary molecular recognition and catalytic properties. (Fersht, 1985) A longstanding goal of enzymology has been to understand how enzymes facilitate the wide variety of chemical reactions found in biological systems from a knowledge of their atomic structures and molecular compositions. Indeed, important insights into the mechanisms of several enzymes have been obtained through the combined use of X-ray crystallography and kinetic, thermodynamic, and genetic engineering experiments. An example of this kind of analysis can be found in the work on triosephosphate isomerase (Albery & Knowles, 1976a; Knowles & Albery, 1977; Nickbarg et al., 1988; Blacklow et al., 1988; Knowles, 1991; Davenport et al., 1991). Despite the substantial progress made, some key aspects of enzyme-catalyzed reactions, such as the atomic, electronic, and energetic characteristics of the reaction mechanism, remain just beyond the reach of present-day biophysical and biochemical experimental methods. In this paper, we describe a theoretical first-principles approach, which is intended to bridge some of the gaps in our understanding of enzyme reaction mechanisms. We demonstrate the utility of this method by analyzing the proton and hydride transfer reactions catalyzed by the enzyme malate dehydrogenase (MDH).[1]

MDH catalyzes the interconversion of malate and oxaloacetate in the citric acid cycle. The arrangement of key catalytic groups in the active site is depicted schematically in Figure 1. We derived our protein model from a 1.9 Å resolution structure of *Escherichia coli* MDH (Hall & Banaszak, 1993) complexed with the substrate analog citrate and the cofactor nicotinamide adenine dinucleotide (NAD). This crystal structure and other biochemical data (Parker et al., 1978; Lodola et al., 1978) indicate that a proton (denoted as H2 in Figure 1) is transferred between the substrate (O2) and His-177 (NE2) in the enzyme and a hydride anion (H21) is transferred between the substrate (C2) and NAD (C4N). Details of the MDH mechanism, which include the order of the reaction (i.e., proton followed by hydride, hydride followed by proton, or concerted) and quantitative information about the structures and energetics of the transition state(s), cannot be determined from the crystal structure or enzyme kinetics experiments. The X-ray structure of the

---

[†] This work was supported in part by the U.S. Department of Energy Office of Health and Environmental Research, under Contract W-31-109-Eng-38.

* To whom correspondence and reprint requests should be addressed.

[‡] Argonne National Laboratory.

[§] M. A. Cunningham Associates.

[||] Yale University.

[⊥] InPharmatics Corp.

[#] Cornell University.

[⊗] Abstract published in *Advance ACS Abstracts,* April 1, 1997.

[1] Abbreviations: AM1, Austin model 1, semiempirical quantum-mechanical model; *d*(X−Y), distance between atoms X and Y; DFT, density functional theory; HF/6-31G(d), Hartree−Fock basis set; k_{cat}, catalytic constant; K_m, Michaelis constant; LDH, lactate dehydrogenase; MDH, malate dehydrogenase; MD, molecular dynamics; MM, molecular mechanics; MP2, Møller−Plesset second-order correlation correction; PM3, semiempirical quantum-mechanical model; NAD, nicotinamide adenine dinucleotide; QM, quantum mechanics; QM/MM, hybrid computational model using quantum mechanics for some atoms and molecular mechanics for the remainder; S_N2, bimolecular nucleophilic substitution reaction; TIP3P, molecular mechanics water model.

S0006-2960(96)02734-1 CCC: $14.00

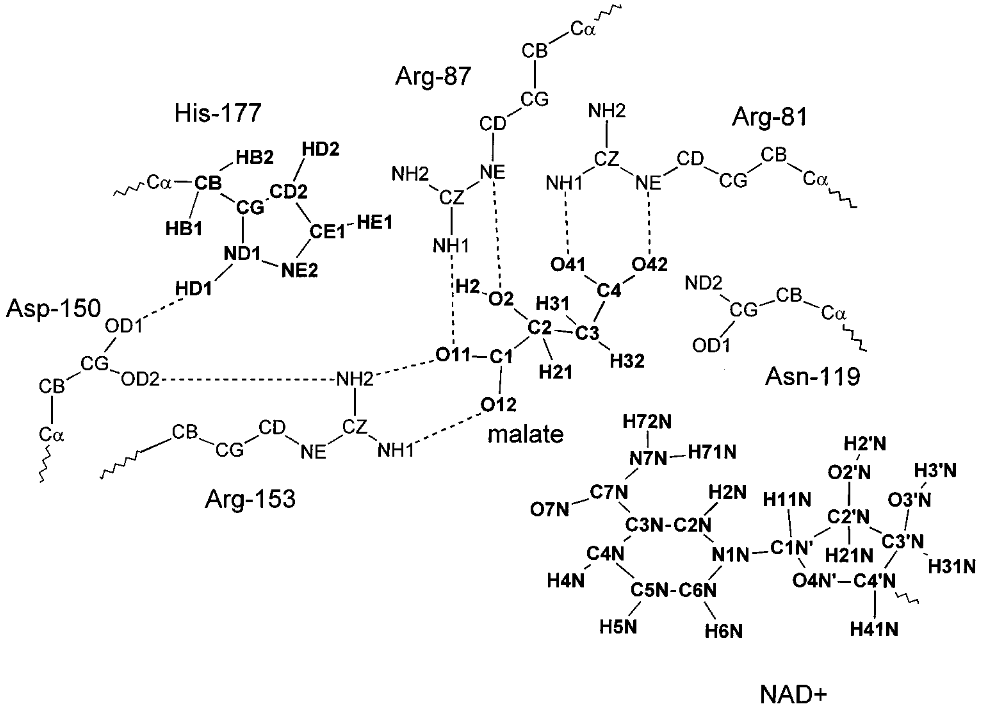

FIGURE 1: Model of the MDH•NAD•malate active site depicting key functional groups. Atoms in the QM partition are labeled in boldface. Dotted lines indicate some of the important hydrogen bonds.

citrate-inhibited ternary complex is a static model of the Michaelis complex, and the rate-limiting step of the MDH reaction is not the proton or hydride chemical transformations. Rather, experimental evidence indicates the rate-limiting step is either the release of NADH or a conformational change that brings the MDH residues Arg-81 and Arg-87 into hydrogen-bonding contact with the substrate in the ternary complex (Lodola et al., 1978). It is, therefore, difficult to obtain details about the chemical events from kinetic or X-ray crystallographic experiments alone.

To address these mechanistic issues, we use a hybrid, quantum, and molecular mechanical (QM/MM) model (Field et al., 1990), which is similar in concept to, but differs in implementation from, methods introduced previously (Warshel & Levitt, 1976; Singh & Kollman, 1986). The model is based on fundamental chemical principles, and it is reliant only upon a knowledge of the chemical composition and the three-dimensional atomic structure of the enzyme–substrate complex. Because a complete quantum-mechanical treatment of macromolecular systems is beyond the capability of present-generation computers, the method circumvents this difficulty by treating only a small number of atoms in the active site quantum mechanically (Dewar & Zoebisch, 1985); the remainder are represented by a classical molecular mechanics model (Brooks et al., 1988). This strategy reduces the computational burden significantly and, as we shall demonstrate, allows a reasonable simulation of even a large system like the MDH•NAD•malate complex. In this paper, we discuss the proton and hydride transfer reactions catalyzed by MDH. We calculate (1) the minimum energy surface with respect to relevant reaction coordinates, (2) the minimum energy pathway for proton and hydride transfers, (3) the transition states along the reaction pathway, and (4) the energetic contributions of the protein matrix in general and specific amino acids and the cofactor NAD in particular to the realization of the catalytic properties of MDH. From the results of these simulations, we propose a detailed reaction mechanism for MDH.

Table 1: Kinetic Properties of Native and Mutant Enzymes[a]

	pyruvate			oxaloacetate		
	k_{cat} (s^{-1})	K_m (mM)	k_{cat}/K_m ($M^{-1}\,s^{-1}$)	k_{cat} (s^{-1})	K_m (mM)	k_{cat}/K_m ($M^{-1}\,s^{-1}$)
native MDH			1.4×10^{-1}	931.0	0.04	2.3×10^{7}
mutant MDH	3.3	25.0	1.3×10^{2}	0.77	3.0	2.6×10^{2}
native LDH	250.0	0.06	4.2×10^{6}	6.0	1.5	4.0×10^{3}
mutant LDH	0.9	1.8	5.0×10^{2}	250.0	0.06	4.2×10^{6}

[a] Data for MDH are from Nichols et al. (1992) and for LDH from Wilks et al. (1988).

The results reported in this work represent a preliminary step in our efforts to develop analytical and predictive numerical tools for use in studying the effects of site-specific mutations in enzymes. In particular, we are motivated by the asymmetric results obtained in MDH and a similar enzyme lactate dehydrogenase (LDH), which facilitates the interconversion of lactate and pyruvate. The observed kinetic properties of both enzymes for pyruvate and oxaloacetate substrates are summarized in Table 1. Conversion of a single glutamine residue to arginine in the native LDH (Gln-102 → Arg) created a mutant which acted as an effective MDH (Wilks et al., 1988). The k_{cat}/K_m ratio of mutant LDH for oxaloacetate substrate is roughly equivalent to that of the native MDH. The converse mutation, replacing the equivalent arginine residue in MDH (Arg-81) with a glutamine was also performed (Nicholls et al., 1992) but with rather different results. The ratio of k_{cat}/K_m in the native and mutant MDH for pyruvate substrate changed by 3 orders of magnitude but is significantly smaller than that observed in the native LDH.

The ability to quantitatively assess the differences between these two mutagenesis experiments is important for the development of predictive theoretical methods that complement enzyme design experiments. In the particular case of the MDH arginine to glutamine mutant, the difference in

k_{cat}/K_m ratios between native and mutant enzymes for oxaloacetate substrate can be interpreted (Nicholls et al., 1992) as a 7 kcal/mol difference in the relative binding energies of the transition states of the enzyme−substrate complexes ΔG^{TS}_{rel}, where $\Delta G^{TS}_{rel} = -RT \ln[k_{cat}/K_m{}^{mutant}/k_{cat}/K_m{}^{native}]$. These experiments provide a useful test case to evaluate the ability of our computational methods to calculate a quantity that can be directly related to the efficiency of an enzyme, i.e., k_{cat}/K_m.

It is possible to calculate ΔG^{TS}_{rel} using free energy perturbation methods (Bash et al., 1987a). However, one must first determine the transition state for the chemical transformations involved with the reaction for both native and mutant enzymes. In this paper, we describe a procedure to determine the transition state for the enzyme reaction in MDH. The resultant analysis of the energy surface for the proton and hydride transfer reactions will be used in subsequent simulations to determine the relative free energies of binding transition states for the native and mutant MDH.

EXPERIMENTAL PROCEDURES

In the QM/MM method, the atomic system is partitioned into regions in which the atoms will be treated either quantum mechanically (QM) or molecular mechanically (MM). Atoms in the two partitions are coupled through electrostatic and van der Waals interactions. Energies $E_{QM/MM}$ for atoms in the QM partition are given by the expectation values of the QM Hamiltonian. Forces $\mathbf{F}_{QM/MM}$ on atoms in the QM partition are obtained from spatial derivatives of the QM Hamiltonian, and combined with the forces $\mathbf{F}_{MM}$ on atoms in the MM partition, energy minimization and classical molecular dynamics (MD) calculations are performed in a standard manner (Brooks et al., 1988). The utility of this QM/MM approach in studying complex condensed phase reactions has been demonstrated by simulations of reaction pathways in solution (Bash et al., 1987; Gao & Xia, 1992, 1993) and by the simulation analysis of the enzyme reaction in triosephosphate isomerase, where a novel mechanism was suggested (Bash et al., 1991) and subsequently verified by experiment (Knowles, 1991).

We utilized a semiempirical AM1 Hamiltonian (Dewar & Zoebisch, 1985) for atoms in the QM partition. The accuracy of the semiempirical Hamiltonian for the proton and hydride transfers in MDH was assessed by the following calculations. Reaction energy profiles for proton and hydride transfers in small model systems that represent the key functional groups were computed at the semiempirical AM1 and *ab initio* MP2 levels of theory using the program Gaussian92 (Frisch et al., 1992). The proton transfer reaction in the MDH·NAD·malate complex was characterized by a proton transfer reaction between methanol and imidazole; the model geometry and results are illustrated in Figure 2a. Similarly, the hydride transfer reaction in the MDH·NAD·malate complex was characterized by a hydride transfer between methanol and protonated pyridine; the model geometry and results are illustrated in Figure 2b. In both cases, the AM1- and *ab initio*-derived structures along the reaction pathway agree to within 0.05−0.1 Å for donor−hydrogen and acceptor−hydrogen distances. Because structures determined through the use of *ab initio* methods generally agree well with experiment (Hehre et al., 1986), we interpret these results to indicate that conformations of states along the reaction pathways are represented reasonably well even at the AM1 level of theory. On the other hand, reaction pathway energetics differ by about 5 kcal/mol, which implies that the AM1-derived reaction activation energies cannot be used to obtain quantitative insights into absolute rates of reaction.

An important component of the QM/MM method is the inclusion of solvent effects due to the environment, which are represented by QM/MM nonbonded interactions. In a related study (Ho et al., 1996), we described the details of a systematic calibration and parametrization process for interaction energies of functional groups of the MDH reaction with water. This involved optimization of the van der Waals parameters used for atoms in the QM partition, with the final result that interaction energies between a water molecule probe and specific atoms of the solute-matched values were determined using *ab initio* methods at the HF/6-31G(d) level of theory to within 0.5 kcal/mol. The HF/6-31G(d) level of theory has been shown to reproduce the interaction energies for hydrogen-bonding complexes of water with organic molecules with good accuracy (Hehre et al., 1986; Pranata et al., 1991), in part due to accidental cancellations between basis set limitations and higher order corrections. Nevertheless, use of this basis set provided a reasonable standard for our calibration of QM/MM interactions. The derived QM/MM model was then applied in the context of bulk aqueous solvent: proton and hydride transfer free energies were calculated for the MDH reaction components represented by small-molecule analogs of malate (methanol), deprotonated malate (methoxide), oxaloacetate (formaldehyde), His-177 (imidazole), protonated His-177 (imidazolium), NAD (protonated nicotinamide), and NADH (1,4-dihydronicotinamide), which are the key functional groups of the enzyme involved in catalysis. The calculated free energies were 15.1 kcal/mol for the proton transfer reaction and −6.3 kcal/mol for the hydride transfer reaction. As noted by Warshel (1980), when proton transfer reactions take place in a polar solvent, the charges are shielded by solvation shells, and even though the physical displacement of the proton is relatively small, the free energy change is equivalent to the case in which the proton is removed to infinity. Consequently, it is possible to directly compare these theoretical estimates of free energy changes with experimental values derived from measurements of pK_a's and redox potentials, e.g., $\Delta G = -2.3RT[pK_a(\text{imidazole}) - pK_a(\text{malate})]$. From the experimental measurements of the pK_a's of methanol (Maskill, 1989) and imidazole (Dawson et al., 1986), we find a free energy change of 12.8 kcal/mol for the proton transfer reaction. As we describe in more detail later, using the redox potentials of ethanol, acetaldehyde, NAD, and NADH (Fasman, 1976), the estimate of the free energy change associated with the proton transfer and recourse to the thermodynamic cycle, we obtain a free energy change of −7.4 kcal/mol for the hydride transfer reaction. These values compare quite well with our theoretical estimates.

We should also note that the solvent has a significant effect on the energetics of the system. In the case of the proton transfer reaction, for which experimental heats of reaction in the gas phase are available from the heats of formation of the reactants and products (Lias, 1988), $\Delta\Delta H^0_f = 157$ kcal/mol. With respect to the gas phase, the effects of water solvation on the energetics of these reacting species is

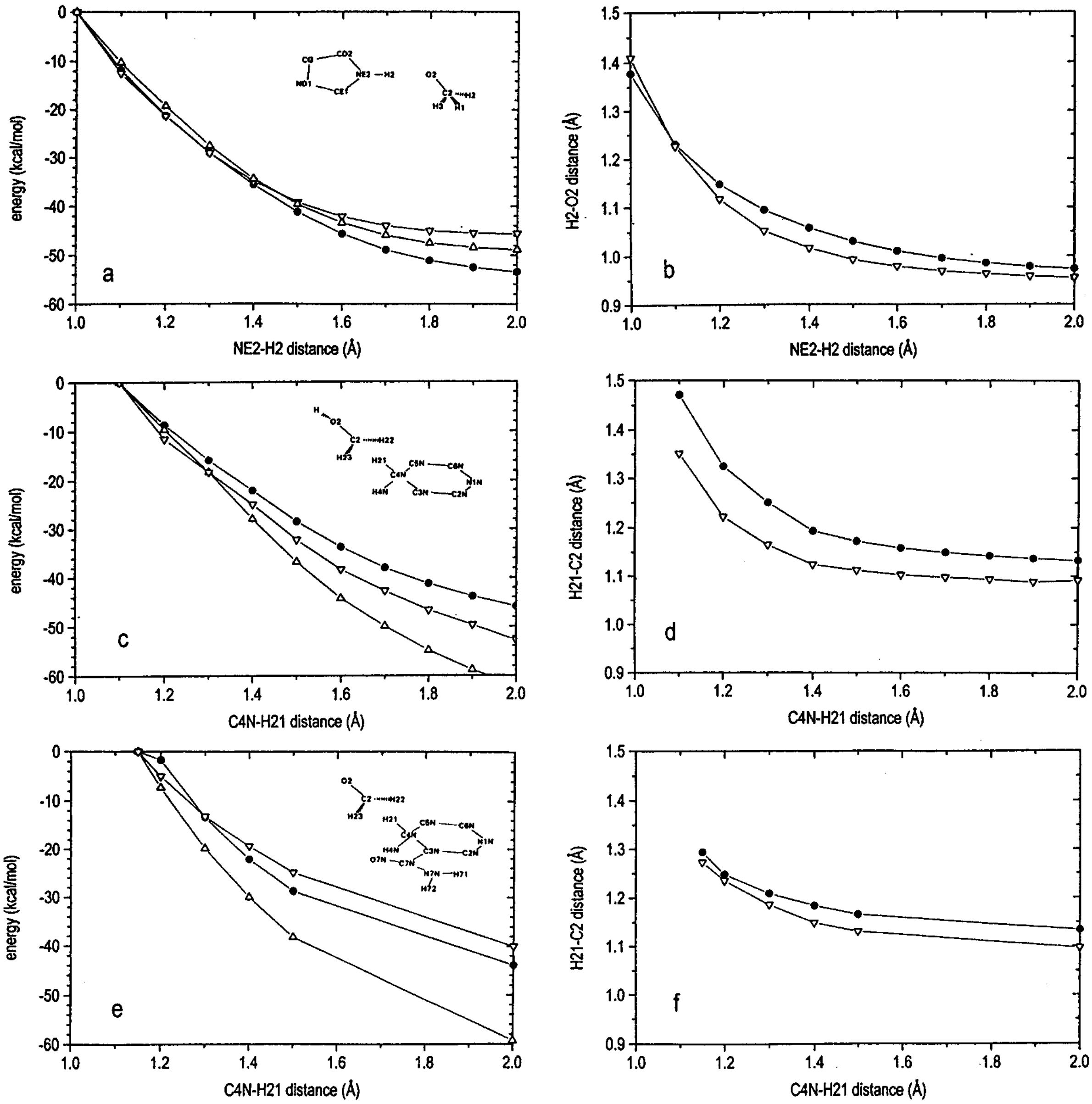

FIGURE 2: Reaction dynamics of small-molecule analogs. Closed circles represent AM1 calculations. HF/6-31G(d) results are denoted by open triangles and MP2 results by down triangles. Panels: (a) energies for proton transfer from imidazole to methanol, (b) donor atom distances for the same reaction as (a), (c) energies for hydride transfer from methanol to protonated pyridine, (d) donor atom distances, (e) energies for hydride transfer from methoxide to protonated pyridine, and (f) donor atom distances. Atom spacings *d*(C4N−H21) and *d*(NE2−H2) are constrained to the ranges of 1.1−2.0 and 1.0−2.0 Å, respectively, in 0.1 Å increments, while allowing the other degrees of freedom to optimize.

dramatic: aqueous solution stabilizes the charged species over their neutral counterparts by about 150 kcal/mol. Warshel (1979) originally demonstrated this effect in the context of the surface-constrained soft-sphere dipole model. Similar solvation effects have since been observed and included in simulations of S_N2 reactions in water by Jorgensen and co-workers (Chandrasekhar et al., 1985). These encouraging results show that the QM/MM method can provide a reasonable depiction of condensed phase reaction phenomena in water. The QM/MM calibration procedure described above is similar to the protocol used to generate nonbonded parameters for the CHARMM MM protein force field, which suggests that our van der Waals parameters generated for QM atoms in a water environment may transfer to the amino acid environment of an enzyme.

We evaluated the transferability of the QM/MM method and parameters for use in the specific environment of the enzyme malate dehydrogenase by the following analysis. The X-ray structure of MDH complexed with citrate (Hall & Banaszak, 1993) suggests that the most important interactions in the enzyme active site are between (1) the carboxylate of Asp-150 and the imidazole ring of His-177, (2) the guanidinium groups of Arg-81 and Arg-153 with the carboxylates of malate, and (3) the guanidinium of Arg-87 with the hydroxyl group of malate and the carbonyl oxygen group of oxaloacetate. Potential energy surfaces were calculated for small-molecule analogs for each of these interactions. Figure 3a−g depicts the molecules and orientations used and the resultant potential energy surfaces. We utilized both MM calculations and a density-functional theory method (DFT) as a standard for comparison with our QM/MM interaction energies. The MM nonbonded electrostatic and van der Waals parameters, which have been generated using an analogous procedure to our QM/MM calibration process,

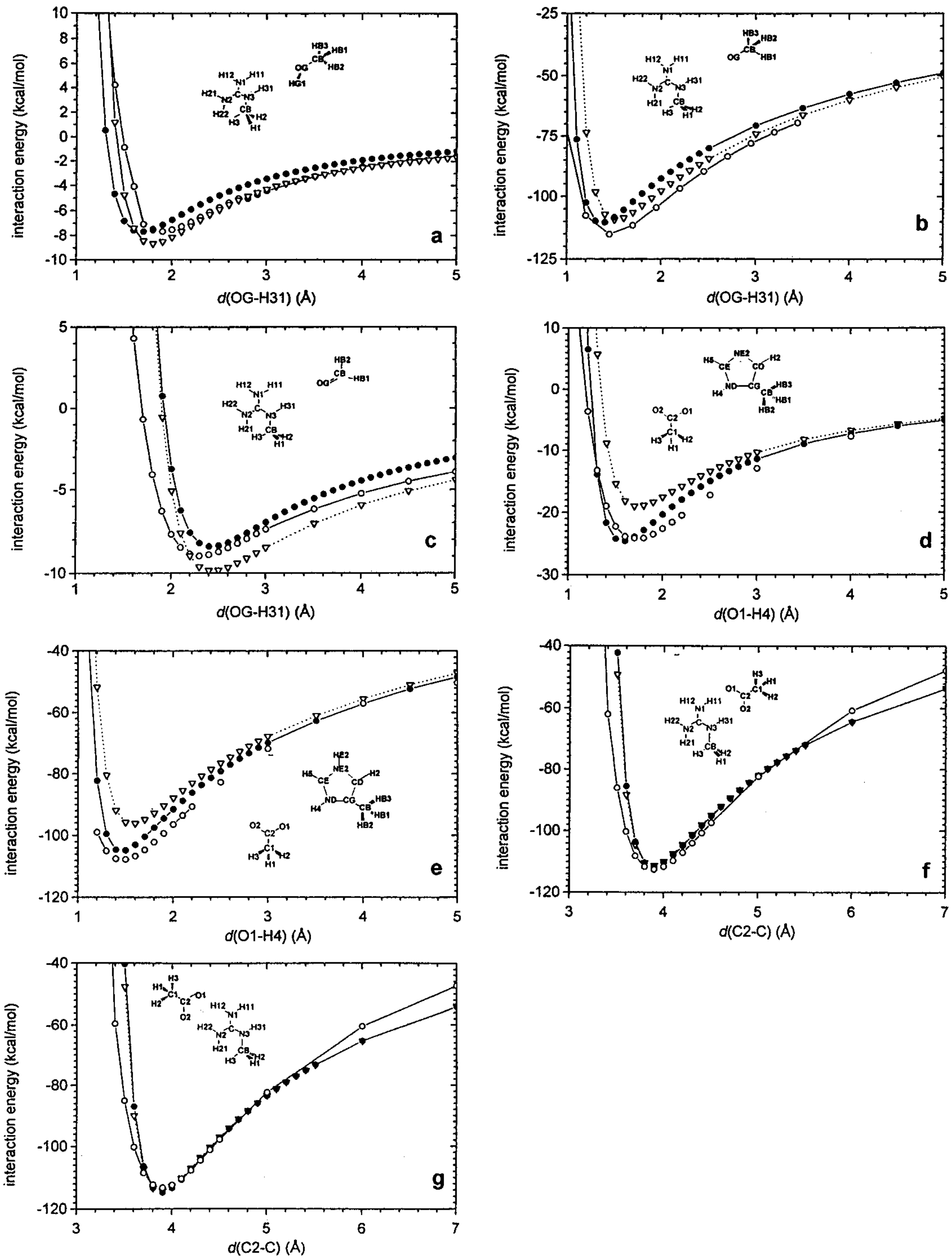

FIGURE 3: Potential energy surfaces between functional groups of the MDH active site. Each monomer was optimized in vacuum to determine its energy and structure using AM1 QM, CHARMM MM, and DFT methods. Complexes were formed in the orientations indicated, and potential energy surfaces were calculated for (a) methanol and methylguanidinium, (b) methoxide and methylguanidinium, (c) formaldehyde and methylguanidinium, (d) acetate and methylimidazole, (e) acetate and methylimidazolium, (f) acetate and methylguanidinium, and (g) acetate and methylguanidinium. QM/MM values are represented by closed circles, MM/MM values by open triangles, and DFT values by open circles. Atoms depicted in boldface were in the QM partition in the QM/MM calculations. Note that in (c) the formaldehyde is oriented at an angle of 115° to the plane of the methylguanidinium.

have been shown to consistently reproduce experimental condensed phase data (MacKerell & Karplus, 1991; MacKerell et al., 1995). The DFT calculations were carried out using the TurboDFT program (Biosym Technologies). Here we used the B3PW91 nonlocal functional proposed by Becke (1993) with the DZVP basis set (Godbout et al., 1992). This nonlocal functional accurately describes weak molecular interactions in hydrogen-bonding systems (Chojnacki et al., 1995).

Figure 3a depicts the interaction energy surface for methylguanidinium, in the MM partition, and methanol, in the QM partition. The QM/MM calculations are represented as closed circles, the MM calculations as open triangles, and the DFT calculations as open circles. All three models yield similar results: the minimum energy configurations agree to within about 1 kcal/mol, and the separation distances between the complexes in the minimum energy conformations agree to within about 0.2 Å. These energetic and structural characteristics are similar to our earlier results with a water probe (Ho et al., 1996). Figure 3b represents the interaction of methylguanidinium and methoxide, where methoxide was in the QM partition, for the QM/MM calculations. Here the difference in energies at the minimum is about 5 kcal/mol and the difference in position of the energy minimum conformation about 0.2 Å. For the interaction of methylguanidinium, in the MM partition, and acetate, in the QM partition, depicted in Figure 3c, we find that the energies agree to within 2 kcal/mol, and the spread in separations between energy minima is about 0.3 Å. Panels d and e of Figure 3 show the potential energy surfaces for methylimidazole and methylimidazolium, in the QM partition, interacting with acetate, in the MM partition. In these cases the QM/MM and DFT calculations agree reasonably well but are rather different from the results of the MM calculations. Minimum interaction energies for the MM calculation are higher in these two cases by 9 and 6 kcal/mol, respectively, while the separation distances of the complexes in the minimum energy conformation are similar. These absolute differences between QM/MM and MM interaction energies in these cases are significant, but for our simulations in the enzyme only the relative interaction energies are relevant. Finally, panels f and g of Figure 3 depict the interaction of methylguanidinium, in the MM partition, with acetate, in the QM partition. The van der Waals parameters on the acetate atoms were set to the same values as those used for the acetate group of aspartate and glutamate amino acid residues in the CHARMM MM force field (MacKerell et al., 1992). In these two cases, the agreement between QM/MM and MM interaction energies and structures is excellent, and both agree well with the DFT results.

In sum, the above test cases (Figure 3a−g) indicate that the QM/MM Hamiltonian can be considered well balanced with respect to the MM Hamiltonian, which is used to model most of the MDH•NAD•malate system (54 atoms are treated with QM and 3000 are with MM). In addition, these data provide a rough estimate of the error in our QM/MM method. For relative energy calculations for states along the MDH enzyme reaction pathway, we would expect the worst-case error in energy to be approximately 5 kcal/mol. This finding is consistent with the solution free energy tests described above and the intrinsic energetics depicted in Figure 2.

The ternary complex of *E. coli* MDH•NAD•citrate has been determined by X-ray crystallography (Hall & Banaszak, 1993) to be a dimer (α,*β*) with two identical active sites. This structure, with malate substituted for citrate, is used as the basic input data for our simulations. Because the electronic and structural changes that occur during the chemical transformations in MDH are anticipated to be localized to a region near the substrate and the active site, we constructed a simulation model which includes all the enzyme residues within 18 Å (centered at the C2 carbon atom of substrate malate) of the active site in the α subunit. Specifically, the model used for our simulations included (1) the malate substrate, (2) the NAD cofactor, (3) 2182 atoms from the α subunit and 520 atoms in the *β* subunit of MDH, (4) 39 water molecules deduced from the crystal structure that are within 18 Å of atom C2, (5) 105 waters added to the enzyme model by superimposing a 20 Å ball of TIP3P water (Jorgensen et al., 1983) centered at atom C2 and removing all TIP3P molecules greater than 18 Å from C2 or within 3.1 Å of non-hydrogen protein atoms, substrate, cofactor, or crystal waters and (6) 27 waters added from a resolvation procedure carried out as for (5) but after 40 ps of stochastic-boundary molecular dynamics at 300 K with all atoms fixed except water molecules. In addition to the key functional groups directly involved in the reaction, this model system contains enough of the protein from the α and *β* subunits of MDH to include long-range electrostatic interactions that may contribute to the stabilization of reaction intermediates along the catalytic pathway with the structural features of MDH necessary to keep the catalytic groups in a geometry competent for the reaction. Figure 1 depicts the principal active site residues and their partitioning into QM and MM regions. MM parameters for protein atoms and the phosphate, sugar, and adenine groups of NAD were taken from the CHARMM all-atom force field (MacKerell et al., 1995). Most of the calculations used a QM/MM Hamiltonian, where malate, the side chain of His-177, and nicotinamide with its adjacent ribose group were treated with QM and, therefore, do not need to be described with an MM potential. However, some of our setup simulations used an MM model for these groups. MM parameters for the hydroxyl, carboxylate, and methylene functional groups in malate were generated by analogy with corresponding amino acid functional groups. Those for the nicotinamide portion of NAD were determined through the same fitting procedure that was used to determine CHARMM MM parameters (Pavelites et al., 1997). The generation and testing of van der Waals parameters used for atoms in the QM partition, as mentioned earlier, are described in detail elsewhere (Ho et al., 1996).

Using our calibrated QM/MM Hamiltonian, a reference conformation of the model was generated by the application of molecular dynamics and simulated annealing methods. A deformable stochastic-boundary procedure (Brooks & Brunger, 1985) with a reaction zone of 16 Å and a buffer region of 2 Å (16−18 Å from atom C2 of substrate malate) was used for energy minimizations and molecular dynamics simulations. Harmonic restraints, with force constants derived from the crystallographic temperature factors associated with MDH atoms, were imposed on buffer-zone protein atoms to constrain them to be near their crystallographically determined positions. An unbiased midpoint for the proton and hydride transfers was defined as the reference state and constructed by constraining reaction coordinates *d*(O2−H2), *d*(H2−NE2), *d*(C2−H21), and *d*(H21−C4N), where *d*(X−Y) is the distance between atoms X and Y, to 1.3 Å. SHAKE (Gunsteren & Berendsen, 1977) was used to fix these four reaction coordinates and bond lengths for MM hydrogen atoms to values defined by their MM parameters. All other degrees of freedom, with the exception of harmonic restraints on buffer-zone atoms and those associated with the stochastic-boundary conditions, were unconstrained. A 13 Å nonbonded cutoff distance for MM interactions and no cutoff for QM/MM interactions were used for all calculations.

The reference structure used in our simulation of the minimum energy reaction surface was generated by the following calculations. Using an MM model for all atoms, a molecular dynamics simulation was performed with 2 fs time steps; the MDH system was heated from 0 to 300 K over an interval of 20 ps with atom velocities assigned from a Gaussian distribution every 2 ps in 30 K increments. The system was equilibrated for an additional 80 ps with atom

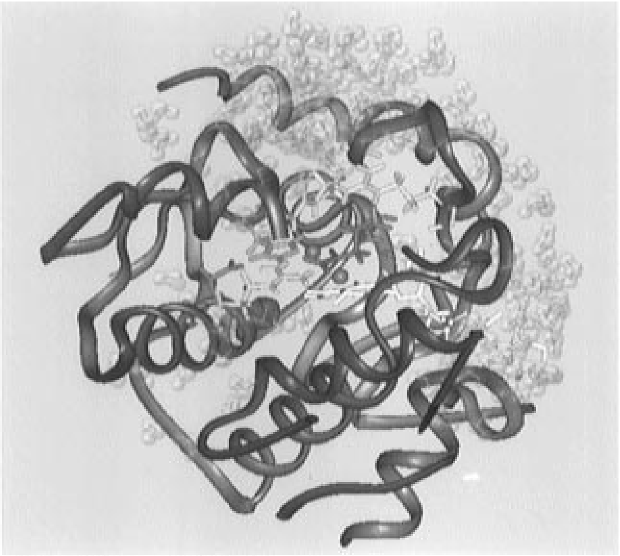

FIGURE 4: Computational model reference structure. The ribbons indicate locations of the α-carbons of the protein residues with a small portion of the loop, representing residues 210−216, excised to reveal the active site. Solvating water molecules are indicated in blue. Key functional groups are color-coded: malate (red), His-177 (green), NAD (yellow), arginine (cyan), aspartic acid (magenta), and asparagine (violet).

Table 2: Root-Mean-Squared Distance Comparison Matrix (Å)[a]

	X-ray	MM av	QM/MM av	QM/MM min
X-ray		0.35 (0.89)	0.34 (0.90)	0.48 (1.00)
MM av	0.35 (0.89)		0.16 (0.39)	0.39 (0.82)
QM av	0.34 (0.90)	0.16 (0.39)		0.38 (0.81)
QM min	0.48 (1.00)	0.39 (0.82)	0.38 (0.81)	

[a] Values in the table are for Cα atoms, with all-atom comparisons given in parentheses.

velocities scaled to maintain a constant temperature of about 300 K. An additional 40 ps of data collection was performed at constant energy with Cartesian coordinates of all atoms saved every 20 time steps for the determination of an average molecular structure $\langle \text{MDH}\cdot\text{NAD}\cdot\text{malate}\rangle^{\text{MM}}_{\text{av}}$. During the data collection phase, the average temperature was 299 ± 4.1 K. A QM/MM molecular dynamics simulation was performed from the end of the MM equilibration stage using the QM and MM partition shown in Figure 1. This simulation utilized 20 ps of equilibration followed by 20 ps of data collection to define a resultant average structure designated as $\langle \text{MDH}\cdot\text{NAD}\cdot\text{malate}\rangle^{\text{QM/MM}}_{\text{av}}$. The temperature during the QM/MM data collection phase was 298 ± 3.9 K.

Finally, a 20 ps annealing simulation from 300 to 0 K was then carried out using the final configuration from the QM/MM data collection phase as an initial starting conformation, and velocities were assigned from a Gaussian distribution at 2 ps intervals in 30 K decrements. The resultant 0 K conformation was energy minimized for 5000 steps to produce the reference structure $\langle \text{MDH}\cdot\text{NAD}\cdot\text{malate}\rangle^{\text{QM/MM}}_{\text{min}}$, which had a final root-mean-squared (RMS) gradient of 0.0001 kcal/Å and an energy change of 0.0005 kcal/mol over the last 100 minimization steps. Figure 4 is a depiction of the $\langle \text{MDH}\cdot\text{NAD}\cdot\text{malate}\rangle^{\text{QM/MM}}_{\text{min}}$ structure in which the α-carbons of the protein residues are illustrated as ribbons. The key residues in the active site are drawn in perspective. Solvating water molecules are also indicated. This structure was used as the starting point for all subsequent calculations carried out to determine the minimum energy surface for the MDH reaction.

Table 2 lists the root-mean-squared distance comparisons among simulated and experimental MDH structures. The similarities between the simulated and experimental structures suggest that (1) the MM Hamiltonian (CHARMM force field) can effectively reproduce the structural features of the MDH active site and (2) the QM/MM Hamiltonian is well balanced and produces the same structural characteristics as the MM representation and the experimental data. This implies that the 18 Å MDH model, the deformable stochastic-boundary conditions, and our QM/MM method together provide a realistic representation of the physical MDH system.

We calculated the minimum energy surface for the hydride and proton transfer reactions in the following manner. Starting from the $\langle \text{MDH}\cdot\text{NAD}\cdot\text{malate}\rangle^{\text{QM/MM}}_{\text{min}}$ structure, we carried out a systematic search over the relevant portions of conformational space associated with the transfer of the proton, H2, from the O2 oxygen of malate to the NE2 nitrogen of His-177 and the hydride, H21, from the C2 carbon atom of malate to the C4N carbon in NAD. This was a four-dimensional search over the distances $d(\text{O2}-\text{H2})$, $d(\text{H2}-\text{NE2})$, $d(\text{C2}-\text{H21})$, and $d(\text{H21}-\text{C4N})$. A 0.2 Å grid spacing was used with a restricted set of configurations of the reaction coordinates defined as follows:

$$0.9\ \text{Å} \le d(\text{O2}-\text{H2}) \le 2.1\ \text{Å}$$

$$1.1\ \text{Å} \le d(\text{C2}-\text{H21}) \le 2.3\ \text{Å}$$

$$0.9\ \text{Å} \le d(\text{H2}-\text{NE2}) \le 2.1\text{Å}$$

$$1.1\ \text{Å} \le d(\text{H21}-\text{C4N}) \le 2.3\ \text{Å}$$

$$2.2\ \text{Å} \le d(\text{O2}-\text{H2}) + d(\text{H2}-\text{NE2}) \le 3.1\ \text{Å}$$

$$2.2\ \text{Å} \le d(\text{C2}-\text{H21}) + d(\text{H21}-\text{C4N}) \le 3.4\ \text{Å}$$

These ranges constitute a physically reasonable ensemble of possible conformations for the interconversion of malate and oxaloacetate. A total of 675 separate energy minimizations, which span the set of parameters defined above, were performed with the same procedure (stochastic-boundary method, cutoffs, and SHAKE) as the molecular dynamics simulations used to generate the $\langle \text{MDH}\cdot\text{NAD}\cdot\text{malate}\rangle^{\text{QM/MM}}_{\text{min}}$ reference structure. A 128-processor IBM SP parallel computer was used with each processor assigned an MDH model with a different and independent set of distance parameters. Each simulation consisted of 1000 steps of the Adopted Basis Newton−Raphson minimization method (CHARMM program). The energy convergence for all 675 minimization calculations was $\Delta E_{\text{min}} = 0.013 \pm 0.03$ kcal/mol, where ΔE_{min} for each calculation was defined as $\Delta E_{\text{min}} = E(\text{step} = 1000) - E(\text{step} = 900)$, and the RMS gradients were 0.001 ± 0.003 kcal/Å.

RESULTS

A minimum energy surface was obtained by projecting out the two degrees of freedom, $d(\text{O2}-\text{H2})$ and $d(\text{C2}-\text{H21})$, that are natural coordinates for the MDH reaction in the direction from malate to oxaloacetate. For each pair of these reaction coordinates, the lowest energy configuration was

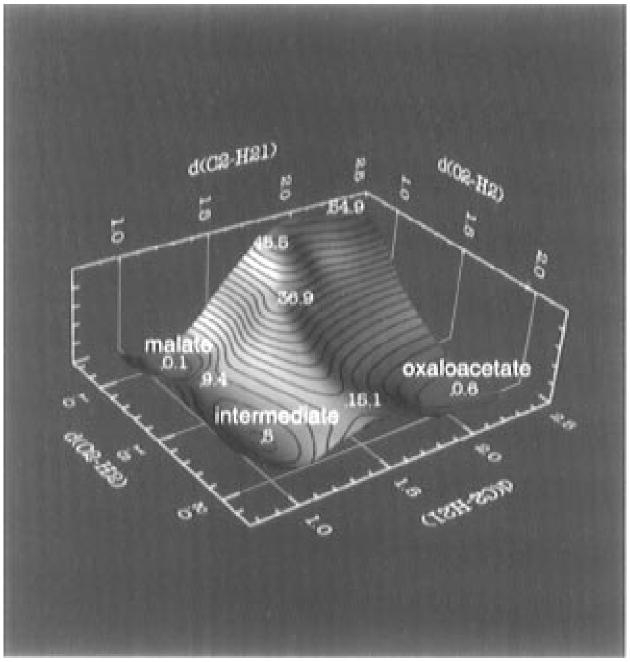

FIGURE 5: Minimum energy surface with respect to MDH reaction coordinates *d*(O2−H2) and *d*(C2−H21), which represent proton and hydride transfers, respectively. Relative energies of the malate, proton transition, reaction intermediate, hydride transition. and oxaloacetate states are indicated.

selected out of the other possible values of *d*(H2−NE2) and *d*(H21−C4N). We observed that the energy difference between the lowest and second lowest energy configurations ΔE_{conf} was much larger than the energy change over the last 100 steps of minimization ΔE_{min} associated with the lowest energy configuration. On average, the ratio $\Delta E_{\mathrm{min}}/\Delta E_{\mathrm{conf}}$ was found to be 0.013 ± 0.023, which indicates that selection of the lowest energy configuration was unambiguous. The result of this projection operation is a minimum energy surface for the MDH reaction, displayed in Figure 5. The first and most obvious result of our simulations can be seen immediately from inspection of Figure 5: the MDH enzyme reaction mechanism appears to be sequential. The proton H2 is first transferred from the O2 oxygen of malate to the NE2 nitrogen of the imidazole ring of His-177 in MDH. The transfer of the hydride anion H21 from the C2 carbon of malate to the C4N carbon of the nicotinamide ring of NAD to produce NADH follows as a separate step. Following this putative path across the energy surface, we note that the initial proton transfer reaction encounters an energy barrier of approximately 7 kcal/mol and the subsequent hydride transfer reaction a barrier of some 15 kcal/mol. This suggests that the hydride transfer may be the rate-limiting chemical step in the reaction.

An alternative reaction pathway, in which the hydride transfer precedes the proton transfer, encounters an energy barrier of some 54 kcal/mol, as noted in Figure 5. The energy difference between this alternate pathway and our proposed path (≈40 kcal/mol) is well within the estimated errors of our method (≈5 kcal/mol) as suggested by the gas phase reaction profiles (Figure 2), the solution proton and hydride transfer calculations (Ho et al., 1996), and tests for transferability of QM/MM parameters (Figure 3). Hence, we are confident in our assessment that we can exclude a reaction mechanism in which the hydride transfer precedes the proton transfer, although it is possible for the reaction to be more concerted than the one suggested by Figure 5. Our ability to precisely determine the reaction pathway is limited by the computational accuracy of the quantum and molecular mechanics Hamiltonians, the fact that we are computing a minimum energy surface and not a free energy surface, and possible discrepancies in our starting conformation. We will discuss these points in more detail later. In addition, the details of this reaction profile may also be influenced by effects due to proton or hydride tunneling, which are not included directly in our calculations. Quantum corrections to our classical potential surface can be estimated using methods similar to those described by Truhlar (Gonzalezlafont et al., 1991) or Warshel (Hwang & Warshel, 1993). Tunneling effects calculated for a similar reaction mechanism in lactate dehydrogenase (Hwang et al., 1991) suggest that quantum corrections may reduce activation barriers for dehydrogenase reactions by about 3 kcal/mol. Although effects due to tunneling may alter the details of our calculated reaction mechanism for MDH, they should have little impact on the overall qualitative features deduced from the simulations.

We define a quadruplet notation to identify individual states in our search space by the following notation S = (*d*(O2−H2), *d*(H2−NE2); *d*(C2−H21), *d*(H21−C4N)), where *d*(X−Y) is the distance in angstroms between atoms X and Y. From our calculated energy surface, we identify five important states: (1) the initial malate state $S_{\mathrm{mal}} = (0.9, 2.1; 1.1, 2.3)$, (2) the proton transition state $S_{\mathrm{proTS}} = (1.3, 1.3; 1.1, 2.3)$, which is determined by the saddle point in the energy surface, (3) the reaction intermediate state after proton transfer is complete $S_{\mathrm{inter}} = (2.1, 0.9; 1.1, 2.3)$, (4) the hydride transition state $S_{\mathrm{hydTS}} = (1.9, 1.1; 1.5, 1.3)$ and (5) the final oxaloacetate state $S_{\mathrm{oxal}} = (2.1, 0.9; 2.3, 1.1)$. Stereoviews of the active site for these five states are depicted in Figure 6.

While the structures illustrated in Figure 6 provide a qualitative overview of the transformation of malate into oxaloacetate, it is possible to elicit more quantitative results from our calculations. In Table 3, we list the interatomic distances for key atoms in the structure for each of the five states defined above. Additionally, we carried out a Mulliken charge analysis (Mulliken, 1955) for atoms in the QM partition and list those results in Table 4. We note, in particular, that the malate substrate is oriented into a configuration amenable for the proton and hydride transfer reactions to occur due to the strong electrostatic interactions formed between the carboxylate oxygen atoms of malate and nitrogen atoms from the guanidinium groups of MDH residues Arg-81 and Arg-153. The hydrogen bonds formed between these groups remain relatively fixed at approximately 2.65 Å throughout the reaction sequence depicted in Figure 6. After the proton transfer has been completed, a net +0.97*e* charge has been transferred to the imidazole ring of His-177; the bulk of the additional charge is localized near the proton (+0.3*e*) and the NE2 nitrogen which accepts the proton. In this reaction intermediate state, the NE2 nitrogen accumulates an additional +0.15*e* over its value in the initial malate state. The CE1 carbon atom of His-177 also becomes more positively charged by about +0.14*e*. This additional charge on the histidine residue is stabilized by the carboxylate oxygen atoms on the adjacent Asp-150 residue; His-177 rotates slightly toward the Asp-150 residue, as can be seen from the decrease in the distance (0.43 Å)

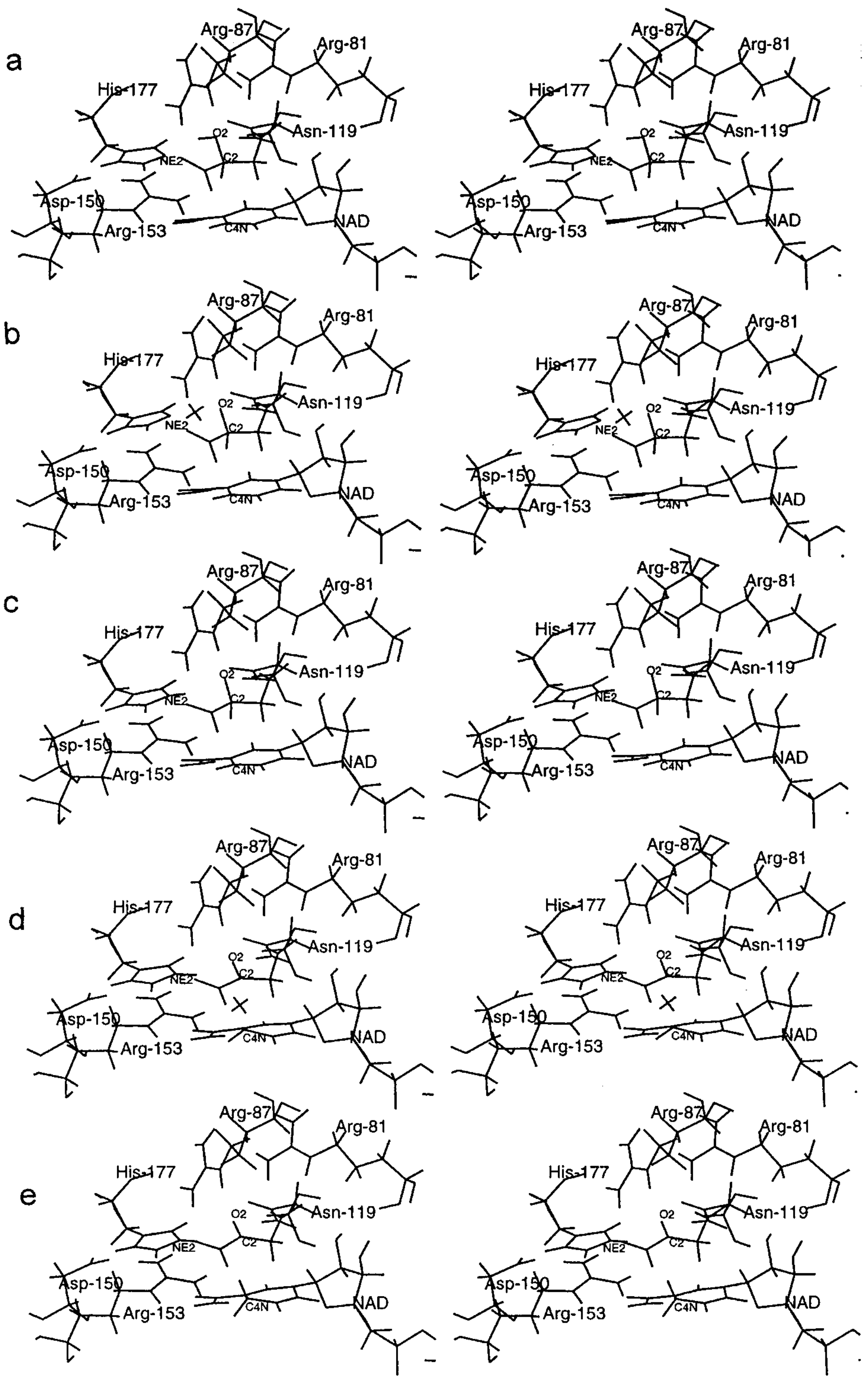

FIGURE 6: Important states on the reaction pathway: (a) malate state, (b) proton transition state, (c) reaction intermediate state, (d) hydride transition state, and (e) oxaloacetate state. The H2 proton and H21 hydride anion are represented as crosses in the transition states.

between the CE1 carbon of His-177 and the OD2 oxygen of Asp-150. The net −0.97*e* charge change on the malate substrate in this reaction intermediate state is concentrated principally on the O2 oxygen atom, which shows a −0.45*e* charge change from its value in the initial malate state. In response, the charge is stabilized by a conformational change that brings the O2 oxygen closer by 0.16 Å to the NE nitrogen in Arg-87 and by 0.42 Å to the ND2 nitrogen of Asn-119. The cofactor NAD is largely unaffected by the proton transfer event.

Between the intermediate state and the final oxaloacetate state, a net charge of −0.99*e* is transferred from the malate substrate to NAD. In the final oxaloacetate state, the charge on the O2 oxygen atom of malate reverts to a value close to that of the initial malate state. We observe that the distances between the O2 oxygen of malate and the NE nitrogen of Arg-87 and the ND2 nitrogen of Asn-119 also relax back to values close to their initial values in response to the reduced charge on the O2 oxygen. The charge transferred to NAD is distributed relatively uniformly around the nicotinamide

Table 3: Interatomic Distances (Å) for Selected Atoms[a]

res:atom	res:atom	mal	proTS	inter	hydTS	oxal	exp
malate:O11	Arg-153:NH2	2.678	2.642	2.637	2.688	2.674	2.69
malate:O12	Arg-153:NH1	2.660	2.671	2.648	2.644	2.649	2.65
malate:O41	Arg-81:NH1	2.660	2.653	2.644	2.650	2.653	2.66
malate:O42	Arg-81:NE	2.650	2.643	2.630	2.647	2.648	2.66
malate:O2	Arg-87:NE	2.635	2.558	2.471	2.919	2.734	3.17
malate:O11	Arg-87:NH2	2.639	2.620	2.631	2.664	2.672	2.65
malate:O2	His-177:NE2	2.946	2.598	2.971	2.938	2.914	
malate:C2	NAD:C4N	3.241	3.252	3.251	2.782	3.330	
malate:O2	His-177:CE1	3.791	3.594	4.034	4.017	3.966	
malate:O2	Asn-119:ND2	3.064	2.896	2.645	2.853	3.140	
His-177:ND1	Asp-150:OD1	2.588	2.567	2.515	2.503	2.504	2.55
His-177:CE1	Asp-150:OD1	3.388	3.356	3.229	3.160	3.193	
His-177:CE1	Asp-150:OD2	3.907	3.723	3.470	3.462	3.521	
Arg-153:NH2	Asp-150:OD2	2.717	2.719	2.723	2.734	2.735	2.72
malate:O12	Wat-662:OH2	2.610	2.607	2.605	2.621	2.626	
malate:O41	Wat-662:OH2	2.706	2.689	2.668	2.708	2.709	
malate:O42	Wat-661:OH2	2.626	2.620	2.604	2.640	2.631	
NAD:O7N	Wat-654:OH2	2.750	2.741	2.756	2.749	2.735	
malate:H2	malate:O2	0.9	1.3	2.1	1.9	2.1	
malate:H2	His-177:NE2	2.1	1.3	0.9	1.1	0.9	
malate:H21	malate:C2	1.1	1.1	1.1	1.5	2.3	
malate:H21	NAD:C4N	2.3	2.3	2.3	1.3	1.1	

[a] Values for the malate (mal), proton transition (proTS), reaction intermediate (inter), hydride transition (hydTS), and oxaloacetate (oxal) states are listed. Experimental values (exp) taken from the MDH·NAD·citrate structure (Hall & Banaszak, 1993) are also listed for comparison. The malate H2 and H21 separations listed in the last four rows of the table were constrained to the 0.2 Å grid. Other atom positions were allowed to vary during the energy minimization process.

ring, and we observe that this charge transfer leaves the charge state of the imidazole ring of His-177 unaffected. The distance between the CE1 carbon of His-177 and the OD2 oxygen of Asp-150 remains relatively constant once the proton transfer is complete and does not change appreciably during the hydride transfer.

The discussions above give a detailed atomic description of the MDH reaction mechanism, but they provide few insights into the reasons why MDH is able to effectively catalyze the interconversion of malate and oxaloacetate. A rationale for the role of protein environmental effects on the catalytic properties of MDH is, however, obtainable through computer experiments using our QM/MM approach. This is accomplished by systematically perturbing the protein matrix, thereby altering environmental effects, and examining the resultant changes in the energetic characteristics of the MDH reaction energy profile. This simulation analysis provides quantitative insights into the role of specific regions in the protein that stabilize or destabilize reactants, intermediates, and products associated with the enzyme reaction mechanism. This kind of information is particularly difficult to obtain with traditional experiments but is a straightforward procedure using computational methods such as our QM/MM technique.

The overall electrostatic solvent effect on the energy profile for the MDH reaction due to the protein matrix was estimated by decoupling the QM and MM interactions. Using the Cartesian coordinates for each conformation associated with the surface of Figure 5, single-point energy calculations were performed for atoms in the QM partition with no MM interactions. The result is shown in Figure 7. This "gas phase" surface indicates that the intrinsic energies for the malate−oxaloacetate reaction are highly exothermic, with the oxaloacetate state preferred by about 54 kcal/mol. From these data, one can see that there is a very strong intrinsic preference for the hydride to transfer from malate to NAD before the proton transfer event. This is completely opposite to the case for the reaction in the protein environment. A closer look at the reacting species suggests a rationale, which is based on an electrostatics argument. The malate has a net charge of $-2e$ due to its two carboxylates. The NAD has a net charge of $+1e$ on the nicotinamide. A hydride transfer will move a pair of electrons from malate to the nicotinamide, which is down an electrochemical gradient from a negative to a positive potential, reducing the charge separation that exists in the reactant state. In the other case, a proton transfer before the hydride will increase the negative charge on the malate anion to $-3e$ and place a $+1e$ charge on the imidazole, resulting in further charge separation, which is a more energetically unfavorable situation. This can be seen in somewhat more detail by inspecting Table 5, in which we list the results of a Mulliken charge analysis for the decoupled reactants. Notably, the charge distribution in the initial malate state indicates that $+0.2e$ of charge has already been transferred to NAD, illustrating the strong electrostatic attraction of NAD for the hydride anion. This is quite unlike the situation in the protein environment, in which NAD is largely unaffected by the initial proton transfer reaction, as is indicated by the charge distributions listed in Table 4. Our calculations, which show dramatic effects due to the enzyme environment of MDH with respect to the gas phase, are similar to ones deduced from the work of Warshel et al. (1989) on other enzyme systems, and they are consistent with observations (Warshel, 1978) concerning the ability of enzymes to evolve unique and effective "solvent" environments.

To ascertain the specific components of the protein environment that contribute to the dramatic energy differences between enzyme-assisted and vacuum reactions, an energy decomposition analysis was also performed. Residues in the MM partition were ordered according to their center-

Table 4: Electric Charge Distributions (*e*)[a]

atom	mal	proTS	inter	hydTS	oxal	atom	mal	proTS	inter	hydTS	oxal
His-177						NAD					
CB	−0.145	−0.156	−0.163	−0.165	−0.166	C1′N	0.111	0.111	0.110	0.146	0.143
HB1	0.094	0.102	0.114	0.119	0.121	H11N	0.129	0.126	0.122	0.090	0.086
HB2	0.075	0.083	0.091	0.095	0.098	C2′N	−0.016	−0.014	−0.015	−0.027	−0.026
HB3	0.089	0.102	0.114	0.111	0.114	H21N	0.124	0.124	0.125	0.121	0.121
CG	−0.156	−0.131	−0.105	−0.092	−0.081	O2′N	−0.372	−0.369	−0.363	−0.377	−0
ND1	−0.174	−0.165	−0.150	−0.144	−0.139	H2′N	0.281	0.283	0.284	0.265	0.262
HD1	0.367	0.388	0.412	0.407	0.416	C3′N	−0.017	−0.018	−0.017	−0.023	−0.022
CD2	−0.192	−0.160	−0.115	−0.113	−0.112	H31N	0.138	0.137	0.135	0.120	0.117
HD2	0.175	0.199	0.230	0.223	0.225	O3′N	−0.360	−0.359	−0.355	−0.350	−0.352
CE1	−0.085	−0.018	0.059	0.056	0.072	H3′N	0.250	0.248	0.245	0.231	0.230
HE1	0.206	0.239	0.271	0.262	0.268	C4′N	−0.056	−0.056	−0.053	−0.049	−0.048
NE2	−0.244	−0.220	−0.090	−0.147	−0.106	H41N	0.113	0.111	0.110	0.097	0.093
						O4′N	−0.282	−0.284	−0.287	−0.295	−0.299
total	0.009	0.262				N1N	−0.053	−0.052	−0.051	−0.210	−0.219
+H2		0.628	0.977	0.968	0.990	C2N	0.025	0.027	0.033	0.053	0.038
						H2N	0.235	0.232	0.228	0.189	0.235
malate						C3N	−0.129	−0.136	−0.139	−0.266	−0.265
O11	−0.660	−0.697	−0.744	−0.684	−0.677	C4N	0.037	0.051	0.062	0.009	−0.049
O12	−0.689	−0.707	−0.725	−0.626	−0.609	H4N	0.217	0.216	0.212	0.133	0.106
C1	0.366	0.351	0.322	0.356	0.351	C5N	−0.158	−0.152	−0.146	−0.244	−0.238
C2	0.028	0.082	0.174	0.272	0.268	H5N	0.211	0.211	0.209	0.163	0.153
H21	0.081	0.028	−0.034	0.007	0.060	C6N	0.016	0.022	0.030	−0.020	−0.041
O2	−0.413	−0.656	−0.857	−0.492	−0.420	H6N	0.217	0.217	0.216	0.174	0.167
H2	0.254	0.366	0.310	0.356	0.280	C7N	0.365	0.363	0.366	0.378	0.377
C3	−0.195	−0.200	−0.221	−0.248	−0.257	O7N	−0.406	−0.422	−0.441	−0.502	−0.5
H31	0.070	0.058	0.045	0.124	0.135	N7N	−0.407	−0.409	−0.410	−0.421	−0.422
H32	0.119	0.102	0.082	0.140	0.154	H71N	0.276	0.279	0.283	0.274	0.274
C4	0.376	0.385	0.395	0.379	0.381	H72N	0.272	0.272	0.265	0.246	0.242
O41	−0.654	−0.665	−0.686	−0.665	−0.664	HCB	0.239	0.240	0.239	0.229	0.227
O42	−0.694	−0.708	−0.722	−0.665	−0.656						
						total	1.000	0.999	0.994	0.133	
total	−2.010	−2.261	−2.261			+H21				0.140	0.005
−H2		−2.627	−2.972	−2.101							
−H21				−2.108	−1.995						

[a] Mulliken charges were obtained for atoms in the QM partition for the malate (mal), proton transition (proTS), reaction intermediate (inter), hydride transition (hydTS), and oxaloacetate (oxal) states. Column sums are indicated for each of the three reactants: His-177, malate, and NAD.

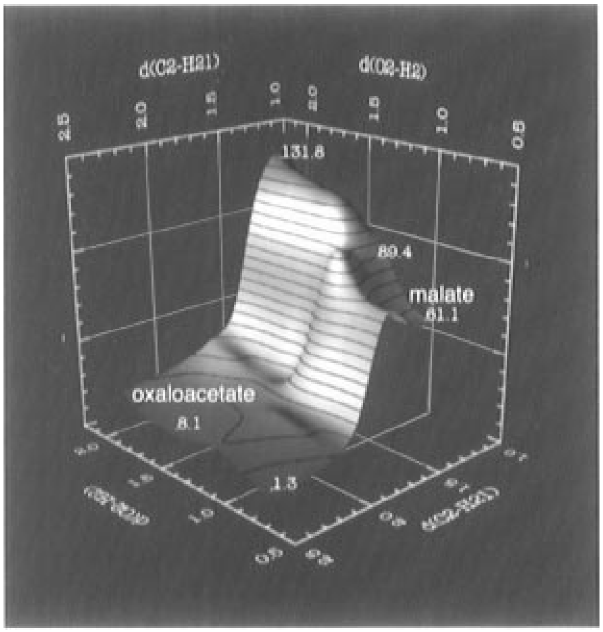

FIGURE 7: "Gas phase" reaction dynamics. Single-point energies for the conformations represented by the minimum energy surface in Figure 5 with the MM energy contribution subtracted. Note the surface is reoriented from that in Figure 5; the hydride reaction in this case proceeds first.

of-mass distance from the C2 carbon atom of malate (center of the local coordinate system). The QM and MM interactions were decoupled for each residue in turn by zeroing the charge on MM atoms and the relative energy contributions computed. We should note that these calculations do not take into account the relative solvation energies of the residues and, therefore, the absolute values of the results serve as a first-order indicator of the effects of solvation due to the environment of the enzyme. Two such energy-difference calculations are shown in Figure 8. The first, the energy difference between the initial malate conformation S_{mal} and the intermediate state S_{inter}, is represented by the open circles. The second, the energy difference between S_{mal} and a state which would represent an initial hydride transfer $S_{\mathrm{H}} = (0.9, 2.1; 2.3, 1.1)$, is represented by the open triangles. The positions of important residues are labeled appropriately. Specific residues in the enzyme have the effect of stabilizing the proton transfer and destabilizing the hydride transfer relative to malate. The largest effects are seen to be due to charged residues within about 10 Å of the C2 carbon in malate. The residues Asp-150 and Arg-87 stabilize the positive charge on the imidazolium of His-177 and the negative charge on the carbonyl oxygen (O2) of malate, respectively, that results from the proton transfer. The residues Arg-81, Arg-153, and Arg-87 provide a large positive potential around the malate, which makes it less advantageous for an electron pair, via the hydride, to transfer from malate to nicotinamide. There are an additional eight negatively charged residues (five Asp and three Glu) and seven positively charged residues (five Lys and two Arg) beyond 10 Å from the C2 carbon atom of malate that are included in the model. These charged residues, as seen from

Table 5: Electric Charge Distributions (*e*)[a]

atom	mal	inter	oxal	atom	mal	inter	oxal
His-177				NAD			
CB	−0.129	−0.152	−0.153	C1′N	0.117	0.137	0.141
HB1	0.080	0.106	0.106	H11N	0.154	0.130	0.122
HB2	0.059	0.084	−0.195	C2′N	−0.008	−0.010	−0.015
HB3	0.077	0.100	0.101	H21N	0.102	0.105	0.105
CG	−0.174	−0.106	−0.102	O2′N	−0.282	−0.294	−0.302
ND1	−0.205	−0.184	−0.185	H2′N	0.253	0.250	0.239
HD1	0.249	0.289	0.290	C3′N	−0.032	−0.033	−0.033
CD2	−0.178	−0.093	−0.090	H31N	0.106	0.093	0.089
HD2	0.161	0.217	0.216	O3′N	−0.304	−0.310	−0.313
CE1	−0.045	0.093	0.108	H3′N	0.220	0.214	0.215
HE1	0.250	0.301	0.299	C4′N	−0.031	−0.027	−0.020
NE2	−0.142	−0.032	−0.029	H41N	0.124	0.112	0.107
				O4′N	−0.294	−0.300	−0.312
total	0.002			N1N	−0.070	−0.139	−0.194
+H2		0.956	0.973	C2N	0.008	−0.033	0.041
				H2N	0.177	0.140	0.126
malate				C3N	−0.128	−0.136	−0.246
O11	−0.560	−0.618	−0.651	C4N	0.050	−0.120	−0.066
O12	−0.593	−0.505	−0.508	H4N	0.229	0.186	0.098
C1	0.319	0.325	0.297	C5N	−0.116	−0.086	−0.159
C2	0.028	0.101	0.222	H5N	0.210	0.177	0.156
H21	−0.011	0.032	0.140	C6N	0.001	−0.083	−0.083
O2	−0.308	−0.525	−0.414	H6N	0.183	0.156	0.140
H2	0.203	0.334	0.324	C7N	0.350	0.355	0.362
C3	−0.179	−0.219	−0.263	O7N	−0.320	−0.397	−0.429
H31	0.016	0.039	0.072	N7N	−0.427	−0.436	−0.442
H32	0.069	0.073	0.104	H71N	0.216	0.223	0.217
C4	0.333	0.335	0.331	H72N	0.238	0.216	0.214
O41	−0.525	−0.559	−0.555	HCB	0.109	0.101	0.099
O42	−0.629	−0.627	−0.606				
				total	0.835	0.191	
total	−1.837			+H21			−0.002
−H2		−2.147					
−H21			−1.971				

[a] Mulliken charges were computed for QM partition atoms decoupled from the MM partition. Values for the malate (mal), reaction intermediate (inter), and oxaloacetate (oxal) states are listed. Column sums are indicated for each of the three reactants: His-177, malate, and NAD.

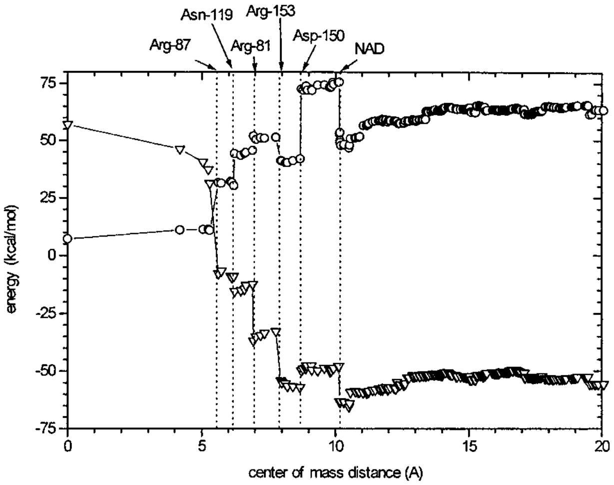

FIGURE 8: Energy decomposition. Residues are ordered by their center of mass distance to the C2 carbon atom of malate. The open circles represent the energy difference between proton transition and malate states, computed by decoupling the QM and MM contributions, and open triangles the difference between hydride transition and malate states.

Figure 8, have little effect on the relative energetics for the proton or hydride reactions.

DISCUSSION

One key aspect of the MDH structure is the precision with which it binds the malate substrate. The carboxylate groups at either end of malate are locked into place by hydrogen bonds with guanidinium groups from arginines of the α subunit of MDH. The O11 and O12 oxygen atoms of malate form a salt bridge with the NH2 and NH1 nitrogen atoms of Arg-153 in a configuration similar to that represented by the acetate−methylguanidinium orientation depicted in Figure 3g. This can be seen in perspective in Figure 6a, and atomic distances are listed in Table 3. Similarly, the O41 and O42 oxygen atoms of malate form a salt bridge with the NH1 and NE nitrogen atoms of Arg-81 in a configuration like that of acetate−methylguanidinium in Figure 3f. All four oxygen−nitrogen distances are approximately 2.65 Å. These strong electrostatic interactions orient the malate substrate in an advantageous position for proton and hydride transfer. From Table 3, we see that the malate O2 oxygen is initially some 2.95 Å from the NE2 nitrogen of His-177 and the malate C2 carbon is initially 3.24 Å from the C4N carbon of NAD. From Table 3, we can also see that the nitrogen atoms NE and NH2 of Arg-87 form hydrogen bonds with the O2 and O11 oxygen atoms of malate, respectively. Interatomic distances for both of these hydrogen bonds are approximately 2.64 Å. Other important functional groups are Asp-150 and Asn-119. The OD1 oxygen of Asp-150 forms a hydrogen bond with the ND1 nitrogen of His-177 (2.59 Å), and the OD2 oxygen of Asp-150 forms a hydrogen bond with the NH2 nitrogen of Arg-153 (2.72 Å). We also note that, in this initial malate state, the distance between the CE1 carbon of His-177 and the OD2 oxygen of Asp-

150 is 3.91 Å. The ND2 nitrogen atom of residue Asn-119 is initially some 3.06 Å from the O2 oxygen of malate. Table 4 lists the charge distributions of atoms in the QM partition. Notably, the −2*e* charge on the malate substrate is largely confined to the carboxylate oxygens (O11, O12, O41, and O42) which have roughly equivalent charges of −0.67*e*. The O2 oxygen of malate also has a large negative charge of −0.41*e*. In the imidazole ring of His-177, the heavy atoms are relatively negatively charged (on the order of −0.2*e*) and the hydrogens relatively positively charged (on the order of +0.2*e*). Charge is distributed in a similar manner on the nicotinamide ring of NAD.

When the enzyme−substrate complex moves to the proton transition state, illustrated in Figure 6b, the O2 oxygen of malate moves to within 2.6 Å of the NE2 nitrogen of His-177 as the imidazole ring rotates upward. The salt bridges between the carboxylate oxygen atoms of malate and Arg-153/Arg-81 remain essentially fixed, with nitrogen−oxygen distances of about 2.65 Å. In the transition state, the NH2 nitrogen of Arg-87 maintains its hydrogen bond with the O11 oxygen of malate, the distance remaining essentially constant at 2.62 Å. The O2 atom of malate has shifted, however, and moves to within 2.56 Å of the NE nitrogen of Arg-87. The ND2 nitrogen of Asn-119 also moves closer to the O2 oxygen, to 2.90 Å. The conformational change also brings His-177 slightly closer to Asp-150, as evidenced by the slightly shorter distance between the CE1 carbon in His-177 and the OD2 oxygen in Asp-150 (3.72 Å). Other hydrogen bond distances remain essentially constant. Together with the conformational changes, the electronic structure of the reacting species begins to reorganize. The largest charge change occurs on the O2 proton−donor atom in malate, which is shown in Table 4 to change from −0.41*e* to −0.66*e*. This increased charge is stabilized by the nitrogens NE of Arg-87 and ND2 of Asn-119, which are closer than in the initial malate state. In the transition state, relatively little charge has been transferred to the imidazole ring of His-177 and, as we noted above, correspondingly small changes in the distance between His-177 and Asp-150. The largest single charge change in the transition state occurs in the CE1 carbon of His-177, which changes from −0.09*e* to −0.02*e*. No appreciable changes occur in NAD.

After the proton transfer is complete, +0.97*e* of charge has been transferred to the residue His-177. This is indicated in Table 4 in the column sum for His-177 designated +H2 (which includes the H2 proton in the column sum). The structure of this reaction intermediate state is indicated in Figure 6c, in which the motion of the His-177 residue, as it rotates back down from its position in the transition state, is apparent. Again, the salt bridges formed between the carboxylate oxygens of malate and nitrogens in Arg-81 and Arg-153 remain fixed at 2.65 Å. The distance between the NH2 nitrogen of Arg-87 and O11 of malate also stays fixed at 2.63 Å. The distance between the NE nitrogen of Arg-87 and O2 of malate, however, decreases to 2.47 Å from its initial value of 2.64 Å in the malate state. Additionally, the distance from O2 of malate to the ND2 nitrogen of Asn-119 decreases to 2.65 Å from 3.06 Å initially. These two residues are ideally positioned to stabilize the increased negative charge on the O2 oxygen, which has risen to −0.86*e* in this intermediate state. In addition, the residue Asp-150 is positioned to stabilize the increased positive charge on the protonated His-177. The OD2 oxygen of the Asp-150 residue maintains a constant hydrogen bond with the NH2 nitrogen of Arg-153, at a distance of 2.72 Å. The Asp-150 residue is strongly affected by the additional charge on His-177, as can be seen in the significant decrease in the distance (to 3.47 Å from 3.91 Å) between the CE1 carbon of His-177 and the OD1 oxygen of Asp-150. The computed charge distribution for atoms in the QM partition indicates that the electronic structure of the protonated His-177 has changed to distribute the additional +0.97*e* about the imidazole ring. This can be seen somewhat more clearly by inspecting Figure 9a, in which we have plotted the charge differences between the initial malate state and the intermediate state. The charge change in the imidazole ring tends to be localized to the vicinity of the proton: the charge on the NE2 nitrogen increases by +0.15*e*, on the CE1 carbon by +0.14*e*, and on the CD2 carbon by +0.08*e*. In malate, the increased negative charge is primarily localized to the O2 oxygen, which changes from −0.41*e* initially to −0.86*e* in the transition state. The H21 hydrogen in malate also becomes significantly negative in the transition state, changing from +0.08*e* in the initial state to −0.03*e* in the transition state. The remaining negative charge is distributed across the malate substrate, with the C2 carbon becoming somewhat more positive, changing from +0.03*e* to +0.17*e*. The NAD cofactor is again unaffected by the proton transfer. In addition to these structural and electronic charge changes, it can be seen from the energy decomposition diagram of Figure 8 that residues Arg-87 and Asp-150 make significant contributions to the stabilization of the charge-separated state that occurs after the proton transfer event. The residue Asn-119 plays a less significant role, due to the fact that it has a net charge of 0 as compared to the net charges of +1*e* for Arg-87 and −1*e* for Asp-150.

At the hydride transition state, the C4N carbon of the nicotinamide ring of NAD and the C2 carbon in malate come within about 2.78 Å of one another, as is illustrated in Figure 6d. Prior to this stage in the reaction, the relative distance had been constant at 3.25 Å. The salt bridges formed by the carboxylate oxygens of malate with nitrogens from Arg-81 and Arg-153 remain fixed at 2.65 Å, as does the distance between the NH2 nitrogen of Arg-87 and O11 of (deprotonated) malate (2.63 Å). The distances between the O2 oxygen of malate and the NE2 nitrogen of Arg-87 and the ND2 nitrogen of Asn-119, however, have increased to 2.92 and 2.85 Å, respectively. Other distances remain essentially constant. Notably, the distances between the ODx oxygens of Asp-150 and heavy atoms in the imidazole ring of His-177 do not change appreciably from their values in the intermediate state. Two electrons transfer with the proton H21, to the nicotinamide ring of NAD, for a net charge transfer of −1*e*. As the electronic structure reorganizes in the transition state, the O2 oxygen of malate begins to lose the negative charge it accumulated after the proton transfer; in the hydride transition state, the charge on the O2 oxygen is −0.49*e*. The nitrogen atoms of Arg-87 and Asn-119 which moved to stabilize the deprotonated malate begin to relax back to their original positions, as we noted above. The charges on the imidazole ring of His-177 are largely unaffected by the hydride transfer, in agreement with our observation that the Asp-150 residue and His-177 appear to have stabilized after the proton transfer was complete. At the hydride transition state, −0.86*e* of charge has been

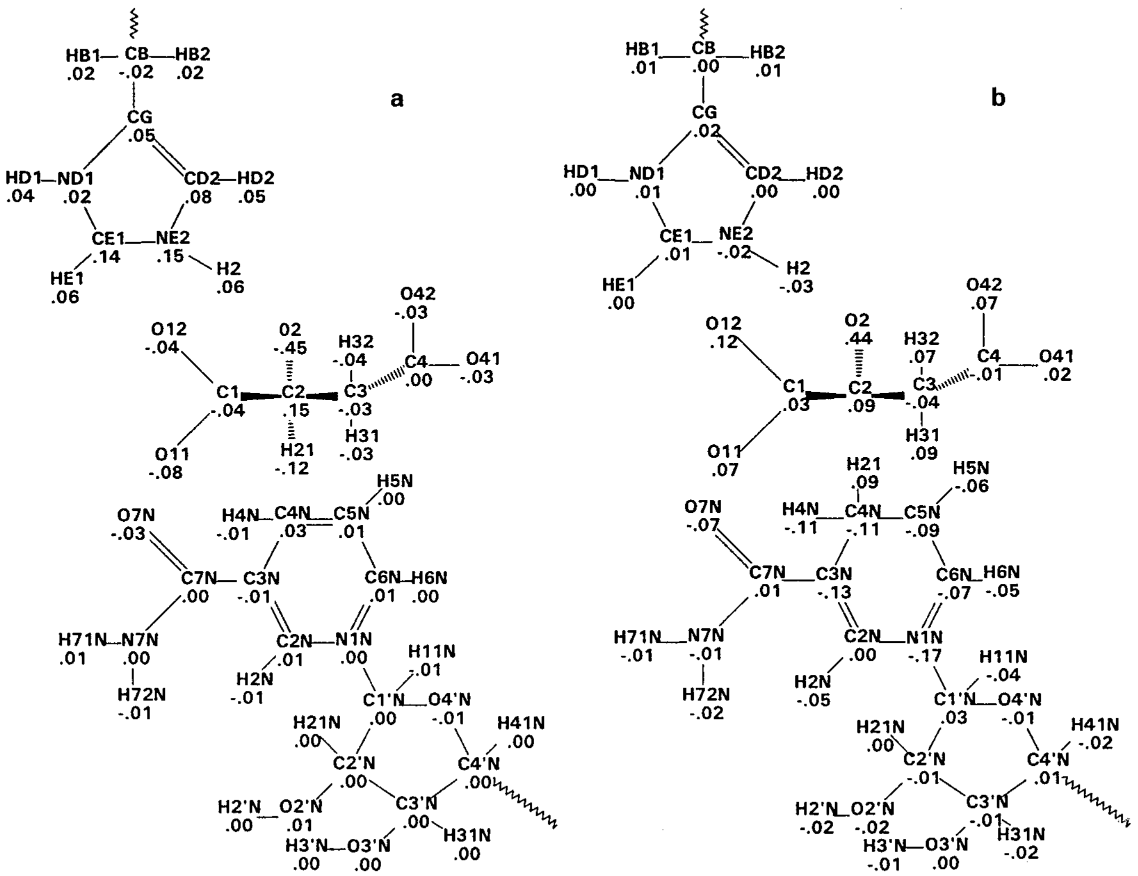

FIGURE 9: Charge distribution changes in the active site. Atoms in the active site are labeled with the difference in their charge states between (a) the intermediate and malate states and (b) the oxaloacetate and intermediate states.

transferred to the nicotinamide ring, distributed relatively uniformly.

In the final, oxaloacetate state, illustrated in Figure 6e, the salt bridges formed by the carboxylate oxygens of malate are still fixed at about 2.65 Å. The hydrogen bond formed by the NH2 nitrogen of Arg-87 and the O11 oxygen of malate has increased slightly, to 2.67 Å, and the distance between the NE nitrogen of Arg-87 and the O2 oxygen of malate has increased to 2.73 Å, slightly larger than the distance in the original malate state. Additionally, the distance between the O2 oxygen and the ND2 nitrogen of Asn-119 has increased to 3.14 Å, close to its initial distance in the malate state. These changes can be largely explained by the observation that the final charge on the O2 oxygen is $-0.42e$, equivalent to the value in the initial malate state. We illustrate the change in charge distribution between the intermediate state, when proton transfer is complete, and the final, oxaloacetate state in Figure 9b. The net charge change of $+1e$ in the substrate includes a $+0.44e$ increase in the charge on the O2 oxygen. Overall, the single largest change in the charge distribution in the substrate between the malate and oxaloacetate states is a $+0.24e$ increase on the C2 carbon. The electronic charge in the nicotinamide ring is distributed relatively uniformly, the largest change occurring for the N1N nitrogen, which changes by $-0.17e$. Little charge was transferred onto the ribose group. We can infer from this observation and the similar observation from Figure 9a, that the CB carbon and HBx hydrogens of His-177 change little during proton transfer, that the ribose group of NAD and the CB-HBx group of His-177 provide a reasonable buffer zone between QM and MM regions.

We have not previously emphasized the role of solvent water molecules on the MDH-catalyzed reaction. Some solvent water molecules are present near the active site and lend hydrogen bonds to important atoms. For example, the O11, O41, and O42 oxygens in malate all share hydrogen bonds with solvent water molecules. While water molecules were not explicitly displayed in Figure 6, we have tabulated some of the relevant distances in Table 4; the interatomic distances remain effectively constant at 2.6 or 2.7 Å, depending on the atoms involved. So, even though water solvent effects are probably not the most important for the proton and hydride transfer reactions, they have not been neglected. Notably, no water molecules appear to make a significant difference in the energy decomposition analysis illustrated in Figure 8.

The minimum energy surface depicted in Figure 5 is key to our analysis. We have used it to define important states along the reaction pathway and can also obtain insights into the energetic effects associated with the environment of MDH relative to aqueous solution. An estimate of the free energy changes in aqueous solution for proton and hydride transfer reactions of the functional groups associated with the MDH reaction mechanism can be obtained from relevant experimental pK_a's and redox potentials. The pK_a of imidazole is 6.04 (Dawson et al., 1986), and the pK_a of the hydroxyl group of malate is about 13.0 (Perrin et al., 1981). Using these values, the free energy for a proton transfer between malate and imidazole in aqueous solution is found from $\Delta G = -2.3RT[\, pK_a(\text{imidazole}) - pK_a(\text{malate})]$ to be 9.6 kcal/mol. An estimate for the corresponding value in the enzyme can be obtained from our minimum energy surface, where we find the energy difference between malate and intermediate states to be about 5 kcal/mol. The enzyme's environment appears to be somewhat more effective than water in the stabilization of an alkoxide intermediate. From the redox potentials for malate and NAD (Fasman, 1976), one can determine the free energy change for the reaction of malate + NAD → oxaloacetate + NADH in aqueous solution to be 6.9 kcal/mol. The free energy change for the hydride transfer reaction of deprotonated malate + NAD → oxaloacetate + NADH is obtained, using the principle of thermodynamic cycles, from the value for the redox reaction, 6.9 kcal/mol, minus the free energy change for the proton transfer reaction (malate + imidazole → deprotonated malate + imidazolium), 9.6 kcal/mol. The resultant free energy change for this hydride transfer reaction in water is thus -2.7 kcal/mol. From our energy surface, we can estimate the free energy change of the hydride transfer reaction to be -4.5 kcal/mol, which again suggests that the protein environment is somewhat more effective than water at stabilizing the charged intermediates. We should note, however, that the overall uncertainty in our calculations of some 5 kcal/mol makes drawing exact conclusions from these results somewhat speculative. Nevertheless, our simulations suggest that the catalytic properties of MDH are due to (1) an environment in the enzyme that produces electrostatic effects similar to those associated with aqueous solution for both the proton and hydride transfers and (2) the orientation of the substrate (malate) relative to catalytic groups (His-177 and the nicotinamide group of NAD) in a geometry which is optimally aligned to facilitate proton transfer from malate to His-177 and hydride transfer from deprotonated malate to nicotinamide.

Earlier computational studies (Wilkie & Williams, 1992; Andrés, 1994; Ranganathan & Gready, 1994) have examined the analogous proton and hydride transfer reactions in the LDH·NAD·lactate system through the use of reduced active site models. In these calculations, all atoms are treated quantum mechanically with AM1 or PM3 (Stewart, 1989) Hamiltonians, and active site residues and substrate analogs are utilized to reduce the computational burden. The calculations range in complexity from formaldehyde interacting with dihydropyridine and imidazole (Wilkie & Williams, 1992) to lactate interacting with 1-methyldihydronicotinamide and 4-methylimidazole (Andrés, 1994; Ranganathan & Gready, 1994). To simulate the effect of the protein matrix, the later studies utilized residue fragments placed in relative positions determined from the experimental crystal structure. For example, arginine residues were represented by 1-methylguanidinium. The general conclusions of these studies were that (i) the hydride transition barrier is larger than the proton transition barrier and (ii) in the direction of lactate → pyruvate, the hydride transfer precedes the proton transfer. While our findings are in agreement with the relative barrier heights for the proton and hydride transfers determined from these cluster studies, we find that the reaction sequence is reversed. Admittedly, these results are for the LDH·NAD·lactate system, not for the MDH·NAD·malate system we investigated, but we find the reversal of the reaction sequence to be somewhat surprising, considering the similarity in the chemistry for the two reactions. As we mentioned previously, it is our intention to investigate the LDH·NAD·lactate system to study the observed asymmetry in site-directed mutagenesis experiments. A more thorough explanation for the differences in reaction mechanisms obtained in our current simulations and those reported previously cannot be definitively evaluated until those studies are completed, particularly since our own observations are that the reaction chemistry in MDH is dramatically affected by the protein matrix.

We mentioned earlier that there are several limitations to our calculations, which necessarily fall far short of a complete quantum mechanical treatment for every atom in the protein complex. The QM/MM method, for example, intrinsically includes the polarization of QM atoms by the protein; the method does not provide for induced polarization of the protein in response to polarization of the QM atoms. We do not believe that this deficiency will qualitatively affect our results. The QM/MM calculations for small-molecule analogs depicted in Figure 3 are in reasonable agreement with the DFT calculations, in which all atoms were treated quantum mechanically and which therefore implicitly include these polarization effects. In addition, we anticipate that some differences will exist between our computed minimum energy surface and the free energy reaction profile; however, the major energy component used in the free energy perturbation method to calculate the potential of mean force along a reaction coordinate (free energy of reaction) is $E_{\mathrm{QM/MM}}$, which we used for our minimum energy surface determination. Additionally, the average potential energy and the free energy for electrostatic interactions (charging process) are related by the linear response approximation (Warshel & Russell, 1984). Our energies for the minimum energy conformations associated with the reaction profile of Figure 5 can therefore be considered to be the relevant average potential energy values. We therefore expect that results from a minimum or a free energy analysis will be qualitatively similar. A detailed comparison of minimum and free energy calculations in the context of MDH is in progress.

Another concern which might be raised about our analysis is the sensitivity of the calculations to the structure of the starting configuration. We attempted to address this issue in the following way. During the 20 ps of molecular dynamics calculations performed to generate the $\langle \mathrm{MDH{\cdot}NAD{\cdot}malate}\rangle^{\mathrm{QM/MM}}{}_{\mathrm{av}}$ structure, we saved the results of the data collection process at 5, 10, and 15 ps into the simulation. Each of these intermediate structures was then annealed and energy minimized in the same way as was performed to create the $\langle \mathrm{MDH{\cdot}NAD{\cdot}malate}\rangle^{\mathrm{QM/MM}}{}_{\mathrm{min}}$ reference structure. In lieu of recomputing the complete energy surface for each of these starting conformations, we instead computed the energies for four states on the minimum energy surface, corresponding to the corners of the surface: S_{mal}, $S_{\mathrm{P}} = (2.1, 0.9; 1.1, 2.3)$, S_{H} and S_{oxal}. Our energy surface calculations suggest that the reaction follows a path that is close to the edge of the surface depicted in Figure 5 and computing the energies at these four points should provide an indication of the sensitivity of our calculations to the initial configuration without the intensive calculations required to reconstruct the energy surface for each starting configuration. Additionally, choosing the corner points as opposed to the minimum energy states provides an additional independent check on the calculations. We list the results of this analysis in Table 6. For different starting conformations, which correspond to reading down the columns in Table 6, we observe that the energy of any given state varies generally within the 5

Table 6: Energies of Reaction Intermediates (kcal/mol)[a]

	S_{mal}	S_{P}	S_{H}	S_{oxal}
5 ps	−567.92	−562.69	−511.35	−570.29
10 ps	−569.31	−562.93	−511.90	−566.22
15 ps	−570.60	−562.07	−519.08	−570.04
20 ps	−571.49	−562.40	−517.79	−570.20

[a] Values of the reaction coordinates for the S_{P} and S_{H} states are S_{P} = (2.1, 0.9; 1.1, 2.3) and S_{H} = (0.9, 2.1; 2.3, 1.1). Structures were developed after every 5ps in the simulated annealing process. The structure created after 20 ps was defined to be $\langle \mathrm{MDH{\cdot}NAD{\cdot}malate} \rangle^{\mathrm{QM/MM}}{}_{\mathrm{min}}$.

kcal/mol estimated precision we have seen in our other tests. We do observe a change of some 7 kcal/mol in one case for the state which represents an initial hydride transfer, which is larger than our estimated errors but also falls in the portion of the surface which is energetically excluded. We note that while details of our analysis may change, our overall conclusions are unaffected by these differences. In all of the starting configurations, corresponding to reading across the rows in Table 6, we see that the final state S_{oxal} is always close to the energy of the initial state S_{mal}, making the reaction nearly isoenergetic in the enzyme environment, independent of starting configuration. Additionally, the initial proton transfer state S_{P} is significantly favored over an initial hydride transfer state S_{H} in all instances.

Finally, calculations of the enzyme reaction in malate dehydrogenase have demonstrated the utility of our approach, which is a general procedure, applicable to the study of any condensed phase reaction. The primary limitation of the method is the accurate and efficient determination of the electronic structures of reacting species, via quantum-mechanical calculations. Although an accurate first-principles calculation of a rate constant is currently beyond the reach of present methods, that situation will undoubtably improve in the not-too-distant future. For the moment, the real power of computer simulation methods is their ability to provide atomic level information and insights into the behavior and properties of physical systems, which are difficult or impossible to obtain from traditional experiments. In MDH, the chemical transformation of malate to oxaloacetate is not the rate-limiting step in the reaction; consequently, details of the reaction dynamics are not accessible to direct experimental examination. It has also proven difficult to predict the effects of site-specific amino acid substitutions in MDH and the related enzyme LDH. Despite similar 3-D structures and chemical compositions of the active sites of MDH and LDH (Hall & Banaszak, 1993; Wigley et al., 1992) it was neither possible, *a priori*, to anticipate the catalytic consequences of these enzyme redesign experiments nor possible, *a posteriori*, to explain them satisfactorily. Development of analytic and predictive computational tools to complement experiment remains a significant motivation for our future efforts.

ACKNOWLEDGMENT

We are indebted to Dr. Mark Donnelly and Dr. Fred Stevens for useful discussions and the suggestion to study the MDH system. We gratefully acknowledge use of the Argonne High-Performance Computing Research Facility. The HPCRF is funded principally by the U.S. Department of Energy Office of Scientific Computing. We also thank two anonymous referees for their constructive criticism of the manuscript.

REFERENCES

Albery, W. J., & Knowles, J. R. (1976a) *Biochemistry 15*, 5627.

Albery, W. J., & Knowles, J. R. (1976b) *Biochemistry 15*, 5631.

Andrés, J., Moliner, V., & Safont, V. S. (1994) *J. Chem. Soc., Faraday Trans. 90*, 1703.

Bash, P. A., Singh, U. C., Langridge, R., & Kollman, P. A. (1987a) *Science 236*, 574.

Bash, P. A., Field, M. J., & Karplus, M. (1987b) *J. Am. Chem. Soc. 109*, 8092.

Bash, P. A., Field, M. J., Davenport, R., Ringe, D., Petsko, G., & Karplus, M. (1991) *Biochemistry 30*, 5826.

Becke, A. D. (1993) *J. Chem. Phys. 98*, 5648.

Blacklow, S. C., Raines, R. T., Lim, W. A., Zamore, P. D., & Knowles, J. R. (1988) *Biochemistry 27*, 1158.

Brooks, C. L., III, & Brunger, A. (1985) *Biopolymers 24*, 843.

Brooks, C. L., III, Karplus, M., & Pettitt, B. M. (1988) *Proteins: A Theoretical Perspective of Dynamics, Structure, and Thermodynamics*, Advances in Chemical Physics, Vol. 71, John Wiley & Sons, New York.

Chandrasekhar, J., Smith, S., & Jorgensen, W. (1985) *J. Am. Chem. Soc. 107*, 154.

Chojnacki, H., Andzelm, J. A., Nguyen, D. T., & Sokalski, W. A. (1995) *Comput. Chem. 19*, 181.

Davenport, R. C., Bash, P. A., Seaton, B. A., Karplus, M., Petsko, G. A., & Ringe, D. (1991) *Biochemistry 30*, 5820.

Dawson, R. M. C., Elliot, D. C., Elliot, W. H., & Jones, K. M. (1986) *Data for biochemical research*, Oxford University Press, New York.

Dewar, M. J. S., & Zoebisch, E. G. (1985) *J. Am. Chem. Soc. 107*, 3902.

Fasman, P. A. (1976) *Handbook of Biochemistry and Molecular Biology*, 3rd ed., CRC Press, Cleveland, OH.

Fersht, A. (1985) *Enzyme Structure and Mechanism*, W. H. Freeman & Co., New York.

Field, M. J., Bash, P. A., & Karplus, M. (1990) *J. Comput. Chem. 11*, 700.

Frisch, M., Head-Gordon, M., Trucks, G. W., Foresman, J. B., Schlegel, H. B., Raghavachari, K., Robb, M., Binkey, J. S., Gonzalez, C., Defrees, D. J., Fox, D. J., Whiteside, R. A., Seeger, R., Melius, C. F., Baker, J., Martin, R. L., Kahn, L. R., Stewart, J. J. P., Topoil, S., & Pople, J. A. (1992) Gaussian 92, Gaussian, Inc., Pittsburgh, PA.

Gao, J. L., & Xia, X. F. (1992) *Science 258*, 631.

Gao, J., & Xia, X. (1993) *J. Am. Chem. Soc. 115*, 9667.

Godbout, N., Salahub, D. R., Andzelm, J. W., & Wimmer, E. (1992) *Can. J. Chem. 70*, 560.

Gonzalezlafont, A., Truong, T. N., & Truhlar, D. G. (1991) *J. Chem. Phys. 95*, 8875.

Gunsteren, W. F. v., & Berendsen, H. J. C. (1977) *Mol. Phys. 34*, 1311.

Hall, M. D., & Banaszak, L. J. (1993) *J. Mol. Biol. 232*, 213.

Hehre, W. J., Radom, L., Scheyer, P., & Pople, J. A. (1986) *Ab Initio Molecular Oribital Theory*, John Wiley & Sons, New York.

Ho, L., MacKerell, A. D., Jr., & Bash, P. A. (1996) *J. Phys. Chem. 100*, 4466.

Hwang, J. K., & Warshel, A. (1993) *J. Phys. Chem. 97*, 10053.

Hwang, J. K., Chu, Z. T., Yadav, A., & Warshel, A. (1991) *J. Phys. Chem. 95*, 8445.

Jorgensen, W. L., Chandrasekhar, J., Madura, J., Impey, R. W., & Klein, M. L. (1983) *J. Chem. Phys. 79*, 926.

Knowles, J. R. (1991) *Nature 350*, 121.

Knowles, J. R., & Albery, W. J. (1977) *Acc. Chem. Res. 10*, 105.

Lias, S. G. (1988) *J. Phys. Chem. Ref. Data 17*.

Lodola, A., Shore, J. D., Parker, D. M., & Holbrook, J. (1978) *Biochem. J. 175*, 987.

MacKerell, A. D., Jr., & Karplus, M. (1991) *J. Phys. Chem. 95*, 10559.

MacKerell, A. D., Bashford, D., Bellot, M., Dunbrack, R. L., Field, M. J., Fischer, S., Gao, J., Guo, H., Ha, S., Joseph, D., Kuchnir, L., Kuczera, K., Lau, F. T. K., Mattos, C., Michnick, S., Ngo, T., Nguyen, D. T., Prodhom, B., Roux, B., Schlenkrich, M., Smith, J. C., Stote, R., Straub, J., Wiorkiewicz-Kuczera, J., & Karplus, M. (1992) *FASEB J. 6*, A143.

MacKerell, A. D., Jr., Wiorkiewicz-Kuczera, J., & Karplus, M. (1995) *J. Am. Chem. Soc. 117*, 11946.

Maskill, H. (1989) *The Physical Basis of Organic Chemistry*, Oxford University Press, New York.

Mulliken, R. S. (1955) *J. Chem. Phys. 23*, 1833.

Nicholls, D. J., Miller, J., Scawen, M. D., Clarke, A. R., & Holbrook, J. J. (1992) *Biochem. Biophys. Res. Commun. 189*, 1057.

Nickbarg, E. B., Davenport, R. C., Petsko, G. A., & Knowles, J. R. (1988) *Biochemistry 27*, 5948.

Parker, D. M., Lodola, A., & Holbrook, J. J. (1978) *Biochem. J. 173*, 959.

Pavelites, J., Bash, P. A., Gao, J., & MacKerell, A. (1997) *J. Comput. Chem.* (in press).

Perrin, D. D., Dempsey, B., & Serjeant, E. P. (1981) *pK_a Prediction for Organic Acids and Bases*, Chapman and Hall, New York, NY.

Pranata, J., Wierschke, S. G., & Jorgensen, W. L. (1991) *J. Am. Chem. Soc. 113*, 2810.

Ranganathan, S., & Gready, J. S. (1994) *J. Chem. Soc., Faraday Trans. 90*, 2047.

Singh, U. C., & Kollman, P. A. (1986) *J. Comput. Chem. 7*, 718.

Stewart, J. P. (1989) *J. Comput. Chem. 10*, 209.

Wang, I. S. Y., & Karplus, M. (1973) *J. Am. Chem. Soc. 95*, 8160.

Warshel, A. (1978) *Proc. Natl. Acad. Sci. U.S.A. 11*, 5250.

Warshel, A. (1979) *J. Phys. Chem. 83*, 1640.

Warshel, A. (1981) *Biochemistry 20*, 3167.

Warshel, A., & Levitt, M. (1976) *J. Mol. Biol. 103*, 227.

Warshel, A., & Russell, S. T. (1984) *Q. Rev. Biophys. 17*, 283.

Warshel, A., Aqvist, J., & Creighton, S. (1989) *Proc. Natl. Acad. Sci. U.S.A. 86*, 5820.

Wigley, D. B., Gamblin, S. J., Turkenburg, J. P., Dobson, E. J., Piotek, K., Muirhead, H., & Holbrook, J. J. (1992) *J. Mol. Biol. 223*, 317.

Wilks, H. M., Hart, K. W., Feeney, R., Dunn, C. R., Muirhead, H., Chia, W. N., Barstow, D. A., Atkinson, T., Clarke, A. R., & Holbrook, J. J. (1988) *Science 242*, 1541.

BI962734N